IMAGING GEOMETRY AND GROWTH RATE OF A HYDRAULIC FRACTURE ZONE BY LOCATING INDUCED MICROEARTHQUAKES

Yingping Li and C. H. Cheng

Earth Resources Laboratory
Department of Earth, Atmospheric, and Planetary Sciences
Massachusetts Institute of Technology
Cambridge, MA 02139

ABSTRACT

The hydraulic fracturing technique has become an important tool in the enhancement of hydrocarbons recovery, geothermal energy extraction, and solid waste disposal. The characterization of geometry parameters and growth rate of a hydraulic fracture zone is an important task for monitoring and assessing subsurface cracks. In this paper, we develop a location approach to determine the precise hypocenter locations for a cluster of seismic events induced by hydraulic fracturing. Two techniques were used in our location scheme: waveform correlation and grid search methods. The waveform correlation method allows us to obtain more accurate differential arrival times among events within in a cluster.. The grid search method is suitable when dealing with a nonlinear location problem.

We applied our method to seismic waveform data from a hydraulic fracturing experiment at the Los Alamos Hot Dry Rock geothermal site and determined hypocenter locations for 157 induced microearthquakes. The maximum absolute and relative location errors were estimated to be 30–39 meters and 3–9 meters, respectively. Among the 157 events, 147 microearthquakes occurred in a tight cluster of a dimension of 40 meters, roughly defining a vertical hydraulic fracture zone. The length, height, and width of the hydraulic fracture zone were measured to be 40, 35 and 5 meters, respectively. The orientation of the fracture zone is estimated at about $N40^oW$. Analysis of the temporal-spatial pattern of the induced microseismicity revealed that the fracture zone grows significantly in a two-hour period during the hydraulic injection. Using seismicity distribution in time and space in this period, we determined that the fracture zone grows toward the northwest along the fracture zone strike with a growth rate of 0.1–0.2 meters per minute.

INTRODUCTION

Hydraulic fracturing for enhancing the recovery of hydrocarbons has been a common reservoir engineering practice since it was first introduced at the Hugoton gas field in western Kansas about a half-century ago (Mahere and Mauk, 1987). This technique has also been extensively used to extract geothermal energy. The Hot Dry Rock (HDR) concept is the extraction of heat energy from the crust in a geothermal area by circulating water through man-made hydraulic fractures between two deep wellbores within otherwise impermeable rock (Harlow and Pracht, 1972). The concept has been successfully tested in some geothermal sites by scientists from several countries (Albright and Pearson, 1982; Cash *et al.,* 1983; Pine and Batchelor, 1984; Majer and Doe, 1986; Talebi and Cornet, 1987; House, 1987; Fehler *et al.,* 1987). Recently, it was proposed that the hydraulic fracturing technique can be safely used for solid waste disposal (The Atlantic Richfield Corporation, 1994). All of these applications require a basic knowledge of the geometry parameters of the hydraulic fracture zone, such as orientation, length, height, width, etc., as well as the characteristics of the fracture growth process.

The seismic monitoring technique is a useful tool for estimating the geometry parameters of a hydraulic fracture zone and has been widely used during a hydraulic fracturing experiment (e.g., Cash *et al.,* 1983; Pine and Batchelor, 1984; Majer and Doe, 1986; Talebi and Cornet, 1987; House, 1987). However, most of these previous investigations focused on the final geometry of a hydraulic fracture zone, rather than on the dynamic growth process of the fracturing. In this paper, we developed a location approach, which takes advantage of the waveform correlation analysis and grid search method, to precisely locate the hypocentral locations for 157 induced microearthquakes which occurred at Fenton Hill, New Mexico, during a hydraulic fracturing experiment in December 1983. By analyzing the induced seismicity pattern in time and space, we determine the orientation, length, height, and width of a hydraulic fracture zone, defined by a tight cluster of microearthquakes, and estimate the growth rate of the fracture zone.

DATA AND METHOD

Experiment 2032 and Waveform Data

The Los Alamos HDR geothermal reservoir is located at Fenton Hill, New Mexico. At the Los Alamos geothermal site, many hydraulic fracturing experiments were carried out to create fracture zones between two deep wellbores. During experiment 2032 in December 1983, approximately 21,600 m^3 of water was continuously injected into a well at a depth of 3460 m below the surface, under a high pumping pressure of about 48 MPa. During the 61 hours of water injection, more than 10,000 microearthquakes induced by hydraulic fracturing were recorded by four borehole seismic stations (House, 1987). The station distribution is shown in Figure 1. The depths are referenced to 2650 m above sea level. Stations EE1, EE3, and GT1 were situated within the Precambrian basement rock, while station PC1 was located within a cavernous limestone formation at a shallower depth. Stations EE1 and EE3 were equipped with triaxial geophones, but stations GT1 and PC1 only had vertical component seismometers.

We obtained seismic waveform data from the Los Alamos National Laboratory for a small subset (cluster B in Figure 1) of the microearthquakes recorded from experiment 2032. The dataset includes waveforms of 176 events recorded at the four borehole stations. These events occurred in a hydrofracture zone and its vicinity during 08:00, December 7, 1983 to 03:00, December 9, 1983. All seismic waveform data were recorded on an analog tape recorder and later digitized at a sampling rate of 5000 samples per second. Spectral analysis of the recorded waveforms (Fehler and Phillips, 1991) indicate that corner frequencies for typical microearthquakes are about 400 Hz, corresponding to wavelengths of 16 m and 9 m for P and S waves, respectively. The best waveform data were recorded at stations EE1 and GT1. Waveforms recorded at station EE3 generally were clipped for larger events, especially for S waves, owing to the short distance from the hydrofracture zone. In contrast, only the larger microearthquakes could be well-recorded at station PC1.

We have used this waveform dataset to measure P and S arrival times and then determine the precise relative locations for 157 microearthquakes which occurred between 08:00 and 20:00, 7 December 1983. All of the events that we relocated have six to eight arrival time readings. For the unclipped waveform data, we applied a waveform correlation analysis technique to refine the picks of the arrival times for P and S waves. For clipped data, especially for S waves recorded at station EE3, a traditional method was used to pick the arrival times. For stations EE1, GT1, and PC1, only vertical component waveforms were used in our correlation analysis. For station EE3, we picked P and S wave absolute arrival times from both vertical and horizontal components and used an average value of the three components as the final reading.

Waveform Correlation and Measurement of Arrival Times

The top frame of Figure 2 shows vertical component waveforms of three microearthquakes recorded at station EE1. We note that the P and S waveforms show a striking similarity from event to event, suggesting that their hypocentral locations are very close to each other, that their focal mechanisms are similar, and that their seismic waves pass through almost identical propagation paths (e.g., Geller and Mueller, 1980). The waveform similarity of these induced microearthquakes allows us to accurately measure the differential arrival times of seismic phases among the events in a cluster using a waveform cross-correlation technique.

The cross-correlation analysis techniques either in the frequency domain (e.g., Poupinet *et al.,* 1984' Ito, 1985; Fremont and Malone, 1987; Moriya *et al.,* 1994) or in the time domain (e.g., Frankel, 1982; Pechmann and Kanamori, 1982; Phillips *et al.,* 1992; Deichmann and Garcia-Fernandez, 1992; Rodi *et al.,* 1993; Li *et al.,* 1995) have been developed to quantitatively characterize the degree of similarity of seismic waveforms from a cluster of earthquakes close in space and to measure their differential arrival times in an accurate, objective, and consistent manner. The conventional time domain analysis typically enables arrival times to be read, at best, to an accuracy of one sample interval, while the cross-spectral method (Poupinet *et al.*, 1984; Ito, 1985) and interpolating techniques in the time domain (Deichmann and Garcia-Fernandez, 1992; Li *et al.*, 1995) can improve the timing precision to about 2 to 10 times better than the sampling interval. For the dataset used in this paper, the sampling interval is quite small (0.2 ms) already and the effect of the uneven velocity of the analog tape playback is about the same order of magnitude. Therefore, we believe a conventional time domain cross-correlation method will provide enough accuracy for our analysis.

Examples in Figure 2 illustrate the procedure we used to measure absolute P and S arrival times and the differential times among the master and slave events with a cross-correlation technique. We selected the event 2967 as a master event because of its suitable size that can be well-recorded at four stations with only S wave being clipped at station EE3. The vertical bars, T1 and T2, in the top frame of Figure 2 mark our preliminary picks of absolute arrival times for P and S waves, recorded at station EE1. We calculated an initial origin time for the event using the picks and a half-space velocity model with $V_p = 5920$ and $V_s = 3500$ m/s (House, 1987). We picked the P and S arrival times at the other three stations, and then calculated the traveltimes of the P and S waves at four stations for the master event with the calculated initial origin time as a reference. The picking errors for absolute arrival times are estimated to be 1 to 2 ms for P and S waves, which is consistent with that estimated by House (1987).

Waveforms of different events observed at each station were preprocessed so that the first P arrivals of all slave events were approximately aligned with that of a master event (Figure 2, top frame). With event 2967 as the master event, we calculated the cross-correlation functions for two slave events 3130 and 3232 using both P and S waveforms. The time windows used for calculating the correlation functions are 20 ms for the P waves and 40 ms for the S waves. The bottom frame of Figure 2 shows the auto-correlation functions for the master event 2967 and the cross-correlation functions for the two slave events, 3130 and 3232. The very high correlation coefficients of 0.8 to 0.9 for both P and S waves indicates that the two events are very close to the master event and the slave and master events have similar focal mechanisms.

We can measure the differential times from the time lags between the maximum peaks of the correlation coefficients. At station EE1, differential time T4-T3 is less than zero for event 3130 and is greater than zero for event 3232, implying that event 3130 is closer to station EE1 and event 3232 is farther away from the station with the master event 2967 as a reference. We assess the reading accuracy of the differential arrival times from correlation functions based on the width of the main correlation peak. For the data processed in this study, the average width between the two 3 dB points of the P wave correlation peaks was approximately 0.8 ms. For S the average is about 1.2 ms. We estimate the error in picking the correlation peaks to be no more than half of the 3 dB widths of the main correlation peak. Therefore, the measurement accuracy of the differential times are estimated typically to be about 0.4 ms for the P waves and

Table 1: Initial Traveltime Station Corrections

	Traveltime correction (ms)	
Station	P	S
EE1	0.6	2.3
EE3	-0.5	-1.5
GT1	-0.5	10.9
PC1	28.9	44.3

0.8 ms for the S waves. With the differential times of the slave events at each station, we can calculate the initial origin times and traveltimes of the slave events using the master event as a reference. For the 157 microearthquakes we analyzed in this paper, we obtained about 1100 preliminary traveltime data, which will be used to invert for the event locations.

Two-Step Grid Search Method

We developed a two-step grid search method to determine the locations of microearthquakes induced by hydraulic fracturing. We adopt the half-space velocity model with $V_p = 5920$ and $V_s = 3500$ m/s and an initial station correction model (Table 1), which are developed by scientists in the Los Alamos National Laboratory based on a few calibration shots and a series of well-recorded events (House, 1987; Phillips *et al.*, 1992). According to this simple velocity model, the calculated P wave traveltimes to stations EE1 and EE3 are 78.4 and 44.8 ms, corresponding to hypocentral distances to the stations of about 465 meters and 265 meters, respectively. It is also known that the injection interval of the experiment 2032 was at a depth of about 3460 m (House, 1987). The information helps us to select a suitable search volume. Using a Cartesian coordinate system shown in Figure 1 (see Block, 1991, for details), we select a volume of 1000 by 1000 by 1000 m, centered at -500 m (East), -300 m (North) and -3400 m (depth), as a target volume to be searched for.

In the first-step grid search, the target volume is divided into 1,000,000 elements of 10 by 10 by 10 m. We put a hypothetical source at each grid and calculated the P and S traveltimes from the source to the four stations and compared with the observed traveltimes, assuming that the origin time is equal to the initial origin time calculated with the P and S arrival times from station EE1. We scanned the whole target volume to determine the approximate location of the global minimum of the RMS error function, which is a summation of residual squares for P and S wave travel times for all stations. Figure 3 shows some results for the master event 2967. A series of contour plots of the RMS misfits between data and calculated traveltimes were plotted at five different depths. The best approximate location of the event is found on the middle frame with the minimum RMS residual of 4.3 ms. As the source depth increases or decreases, the RMS error increases significantly. However, we also note that the locations of the minimum contours in each frame, corresponding to a different depth, do not change significantly, implying that the approximate location for the epicenter is quite stable. One advantage of using the RMS error contours to present the location result is to show both location and associated residual error simultaneously. The purpose of the first step search is to ensure that our final solution for an event location converges to the global rather than local minimum. It also helps to narrow down the target volume for a refined grid search in the second step.

In the second step of the grid search, the search target is reduced to a volume of 100 by 100 by 100 m, centered at the approximate event location determined from the first step search. The search range for the origin time is -2 ms to 2 ms referenced to the calculated initial origin time with the arrival time data of station EE1. The time is gridded on 0.2 ms intervals, and the space is gridded on the cubics of 0.5 by 0.5 by 0.5 m. We searched in the refined four-dimensional parameter space to find the optimal hypocentral location for an event by fitting the calculated traveltimes with observed data. The final hypocenter of an event is determined when the total RMS misfit reaches the minimum. We used this procedure to reliably determine the hypocentral locations and associated residual errors of 157 induced microearthquakes with 6 to 8 traveltime data for each event. The typical total RMS misfit is about 3.5 to 4.5 ms, which includes both velocity model and arrival time picking errors. Although the grid search method does not provide a direct way to estimate the location errors, the residual information gives data variances which can be used to estimate the uncertainty of the hypocenter location with other methods. Therefore, we keep track of total RMS residuals and of residuals at each station for both P and S waves.

Location Error Analysis: Absolute Versus Relative

In the previous section, we used the two-step grid search method to obtain the hypocentral locations for 157 microearthquakes induced by hydraulic fracturing through fitting observed and calculated traveltimes. The typical RMS misfit is found to be about 3.5 to 4.5 ms. This value is about two times larger than the picking errors for absolute arrival times and about 4 to 10 times larger than the picking errors for the relative arrival times. Therefore, this RMS error should include the contribution from both picking error and velocity model uncertainty. Assuming the RMS error to be the data variance for an event close to the centroid of the microearthquake cluster (cluster B in Figure 1), we calculated typical location uncertainties with a singular-value decomposition (SVD) method (e.g., Lawson and Hanson, 1974; Li and Thurber, 1991). The semi-major axis of the epicenter error ellipse is about 9 to 11 meters, while the depth uncertainty is about 25 to 32 meters. The semi-major axis of the error ellipsoid is estimated to be about 30 to 39 meters. We attribute the calculated location error (30 to 40 meters) as an absolute location error, which is the uncertainty of the true absolute location of the event, since it includes both reading errors and velocity model errors.

The purpose of this paper is to image the geometry and growth rate of a small fracture zone. Therefore, we are much more concerned with the relative location error

Table 2: Average Traveltime Residuals at Each Station

	Traveltime residuals (ms)	
Station	P	S
EE1	-1.8±0.4	-4.3±0.6
EE3	-1.0±0.6	-2.6±0.6
GT1	3.0±0.4	-3.3±0.4
PC1	-6.9±0.4	6.2±0.6

rather than with the absolute location error. The previous theoretical analyses (e.g., Jordan and Sverdrup, 1981; Rodi *et al.,* 1993) have shown that differential times are less sensitive to errors in the velocity model used in the location algorithm, and, as a consequence, that the relative locations of events within a cluster can be determined more accurately than their absolute locations. In order to assess the estimates of relative location errors, we examined the residual dataset for each station that resulted from the grid search location procedure. Table 2 shows the averaged residuals at each station for both P and S waves. Thirty events well-recorded at the four stations were used to calculate these average values. The numbers in Table 2 reflect existing systematic velocity model errors which are not completely corrected by the initial station correction model shown in Table 1. We interpret the reason for these systematic errors as follows: First, the initial station correction model is developed based on a few calibration shots and a series of well-recorded events in the entire fracture zones with a volume of 150 by 850 by 950 meters (House, 1987), which is much larger than the dimension of a small fracture zone associated with cluster B we studied in this paper. Therefore, the initial correction model can be thought of as an average model suitable for the entire fracture zone, but it may be slightly biased when it is used in some specific regions, such as where events of cluster B are located. Second, 3-D velocity joint inversion in the HRD test site by Block *et al.* (1994) indicates that the velocity variation is about 15% in the most intensively fractured regions, supporting our argument that a better station correction used for locating events in the cluster B is not necessarily the same as the initial station correction model.

Based on the initial traveltime station correction model in Table 1 and the average residual values at each station in Table 2, we developed a final station correction model for calculating the locations of microearthquakes within the B cluster and its vicinity. Using this final correction model listed in Table 3, we rerun the grid search program and examine the variation of the RMS residuals. It is found that the total RMS residuals reduce significantly to 0.3 to 1.0 ms, which is about 4 to 10 times smaller than those calculated using the initial station correction model. Table 4 lists the total RMS errors and the RMS errors for P and S waves only for 30 events calculated with the initial and final station correction models. The total RMS residuals calculated with the final correction model are comparable to the picking errors for the relative arrival times and we believe that the RMS errors are dominated by the data variances rather than the

Table 3: Final Traveltime Station Corrections

	Traveltime correction (ms)	
Station	P	S
EE1	-1.2	-2.0
EE3	-1.5	-4.1
GT1	2.5	7.6
PC1	22.0	50.5

velocity model error. Assuming the smaller RMS error to be the data variance for an event close to the centroid of the cluster B, the typical relative location error is calculated with the SVD method. The semi-major axis of the epicenter error ellipse is about 1 to 3 meters, and the depth uncertainty is about 2 to 7 meters. The semi-major axis of the error ellipsoid is estimated to be about 3 to 9 meters. We define this location error as the relative location error, which represents the uncertainty of one slave event compared to the master event and other slave events. Table 5 compares the location uncertainties in the absolute and relative sense. It is clearly shown that the relative location error is about 4 to 10 times smaller than the absolute location error, consistent with what was expected from the theoretical analyses mentioned above. Following the detailed discussion about the location errors, we conclude that the absolute location error for the centroid of the cluster B ranges from 30 to 40 meters, while the relative location errors among the events within the cluster are estimated to be about 3 to 9 meters.

RESULTS AND DISCUSSION

Seismicity Distribution and Geometry of a Hydraulic Fracture Zone

Hypocentral locations of 157 induced microearthquakes determined by a grid search approach are shown by three orthogonal views in Figure 4. All of these seismic events are distributed over an area of 70 by 30 meters. The depth range of the events is about 100 meters, from −3270 to −3370 meters. However, except for some 10 scattered events located in the southeast of the area with deeper focal depths, the majority of the microearthquakes are concentrated in a much smaller volume of 40 by 35 by 5 meters. We see that 147 of the 157 events define a tight cluster with dimension of the order of 40 meters. The map view and the BB' cross-section in Figure 4 show that the cluster delineates an approximate vertical plane striking in the northwest-southeast direction. Cross-section AA' and BB' in Figure 4 indicate that the depth range for the tight cluster is about 35 meters. Our location pattern of this cluster agrees excellently with that of the same cluster located by Phillips *et al.* (1992) with a different location algorithm, although our absolute location for the centroid of the cluster is slightly different from what they determined. This difference may be caused

Table 4: Absolute and Relative RMS Error of 30 Microearthquakes

Event	P(ms)	S(ms)	P+S(ms)	P(ms)	S(ms)	P+S(ms)
2967	3.88	4.74	4.33	0.39	0.45	0.42
2727	4.08	4.14	4.11	0.27	0.19	0.24
2728	3.91	4.20	4.06	0.35	0.19	0.28
2732	3.93	4.55	4.25	0.40	0.36	0.38
2774	3.49	3.94	3.72	0.86	1.39	1.16
2782	3.84	4.53	4.20	0.26	0.28	0.27
2788	3.99	4.56	4.28	0.54	0.48	0.51
2798	3.93	3.97	3.95	0.35	0.36	0.35
2839	3.84	4.01	3.92	0.28	0.39	0.34
2880	4.17	4.67	4.43	0.36	0.37	0.36
2888	4.05	4.21	4.13	0.55	0.25	0.43
2897	3.45	4.40	3.96	0.70	0.97	0.84
2902	3.90	4.23	4.07	0.07	0.21	0.16
2940	3.64	4.48	4.08	0.49	0.24	0.38
2980	3.79	4.90	4.38	0.48	0.59	0.54
2994	3.94	4.58	4.27	0.18	0.32	0.26
2997	3.72	3.92	3.82	0.23	0.47	0.37
3023	3.91	3.95	3.93	0.10	0.43	0.31
3031	4.26	8.51	6.12	0.42	0.76	0.61
3035	4.05	4.76	4.42	0.30	0.51	0.42
3041	4.34	5.10	4.74	0.54	0.81	0.69
3095	4.02	4.45	4.24	0.31	0.21	0.27
3115	3.92	4.01	3.97	0.45	0.48	0.47
3130	3.64	4.38	4.03	0.66	0.47	0.57
3166	4.32	4.87	4.60	0.57	0.56	0.56
3280	4.01	3.89	3.95	0.31	0.47	0.40
3534	4.12	4.16	4.14	0.73	0.49	0.62
3600	3.80	4.69	4.27	0.58	0.63	0.60
3722	3.96	3.91	3.93	0.38	0.60	0.50
4643	3.58	3.83	3.71	0.91	1.10	1.01

Table 5: Absolute and Relative Location Errors

	Epicenter ellipse r (m)	Depth error (m)	Hypocenter ellipsoid R (m)
Absolute	9–11	25–32	30–39
Relative	1–3	2–7	3–9

by using different station correction models or different absolute picking errors. Our absolute centroid point shifts from theirs about 20 meters west and 22 meters down in depth, corresponding to a distance of 30 meters between the two centroid points, which is well within the absolute location error bound (30 to 39 meters) we have estimated.

We conclude that the microseismicity within the tight cluster is associated with the hydraulic fracturing on the pre-existing fault(s) or joint(s), as pointed out by Fehler *et al.* (1987). In contrast, the scattering microseismic events in the southeast may not occur on the pre-existing fault(s) or joint(s), although they are also induced by the hydraulic fracturing. The events in the tight cluster clearly define a hydraulic fracture zone, while the scattering events look random in both time domain and space domain. The distribution of microearthquakes in the tight cluster allows us to estimate the geometry parameters of the hydraulic fracture zone. The fracture azimuth is estimated to be about $N40^oW$. The length and height of the fracture zone are measured to be about 40 meters and 35 meters, respectively. The measurement error should be comparable to the relative location errors (see Table 5). Therefore, measurement errors for the length and height are estimated to be about ±3 meters and ±7 meters, respectively. The width of the hydraulic fracture zone is estimated to be 5±3 meters. Even for the lower bound, the width of 2 meters is still much larger than that of any single fracture. Because of the epicenter location precision of 1 to 3 meters, we do not expect to resolve the width of any single fracture. We suggest that the fracture zone consists of multiple subparallel fractures and that the width we estimated with location data is the overall width for a fracture zone rather than for a single fracture.

Temporal-Spatial Variation of Seismicity

We have examined the spatial distribution of the cluster of microearthquakes induced by hydraulic fracturing and estimated the length, height, and azimuth of a hydraulic fracture zone with the seismicity distribution pattern. In this section, we will further check the temporal-spatial variation pattern of microseismicity simultaneously and expect to reveal some information about the dynamic growth process of the hydraulic fracture zone. To the best of our knowledge, few studies have been done to estimate the growth rate of a hydraulic fracture zone with induced microseismicity, although a lot of work has been done to estimate the geometry parameters of a hydraulic fracture zone (e.g., Fehler *et al.,* 1987; House, 1987; Talebi and Cornet, 1987; Phillips *et al.,* 1992; Rodi *et al.,* 1993).

Figure 5 is a series of map views showing the epicentral locations of the 157 induced microearthquakes which occurred between 08:00 and 20:00, December 7, 1983, in six different time windows. The lengths of the time windows are 1, 2, and 5 hours. These plots show clearly the temporal-spatial variation of the induced microseismicity. Only two events occurred within the time frame of 08:00 to 09:00. One of them was located within the hydraulic fracture zone defined in Figure 4. The majority of the events occurred within the fracture zone in the period between 09:00 and 11:00. We note that the length of the seismicity distribution in the time frame of 10:00 to 11:00 is about twice longer than that in the time frame of 09:00 to 10:00 (Figure 5), suggesting that the hydraulic fracture zone is growing. After that time, the numbers of seismic events reduce significantly, but the seismic events which occurred during 11:00 to 15:00 still can barely delineate the hydraulic fracture zone. After 15:00, seismic activity is back to a level similar to that in the time frame of 08:00 to 09:00.

A series of cross-sections (AA' and BB') in Figures 6 and 7 show the temporal-spatial variations of the seismicity induced by the hydraulic fracturing. A significant growth of the fracture zone from 09:00 to 11:00 is also evident on the cross-section AA' along the strike of the fracture zone (Figure 6). The cross-section (BB'), perpendicular to the strike of the fracture zone, indicates that the height of the fracture zone does not significantly vary in the different time frames from 09:00 to 15:00 (Figure 7). We have demonstrated the temporal–spatial variation of the induced microseismicity with three orthogonal views in different time windows and found that the fracture zone had significantly grown during a time interval of 09:00 to 11:00. However, the time window of one hour is too long to obtain a detailed picture of the growth process. Figure 8 shows the frequency of seismic events in a time interval of 20 minutes. We have found that about 80% of the events occurred during 9:00 to 11:00, December 7, 1983, and, after that time, the seismic activity decreased significantly. Therefore, we will use the seismicity in the period with the majority of events to examine the detailed process of the fracture zone's growth and expect to infer the growth rate.

Growth Rate of Fracture Zone Length

Figure 9 shows the epicentral locations of induced microearthquakes which occurred between 09:00 and 11:00 in six different time frames. The time window for each frame is 20 minutes. These seismicity plots clearly demonstrate that the size of the fracture zone gradually increases along the northwest-southeast direction as a function of time. The strike of the subcluster in each frame is similar to each of others. In the first time frame (09:00 to 09:19.9) in Figure 9, we also plotted an event which occurred at 08:26 with a circle, which is the first event that occurred within the hydraulic fracture zone. We assume that the fracture zone growth process starts with this event. Since the majority of the events were located in the northwest of the initiation event, we believe that our assumption is reasonable and that the hydraulic fracture zone grows dominantly toward northwest along a strike of $N40^oW$.

Cross-sections along the strike (AA') in the six time windows (Figure 10) also display the growth process of the hydraulic fracture zone. The seismicity pattern of the subcluster in each time frame varies significantly, and the area of subclusters in each time frame increases as a function of time. The depth distribution of the subclusters indicates that the height of the fracture zone varies from 20 to 30 meters, with maximum height at a 10:00 to 10:20 time frame and minimum height in the first and last frames in Figure 10. The top frame of Figure 11 plots the fracture zone height against time. The variation of the fracture zone height is about 20% during the two-hour period (09:00 to 11:00). The horizontal dimension of the subcluster in each time frame varies from 12 to 32 meters with the minimum horizontal length at a 09:00 to 09:20 time frame and maximum length at the last time frame in Figure 10. Therefore, we conclude that the hydraulic fracture zone grows horizontally mainly towards the northwest.

In order to estimate the growth rate of the fracture zone length, we define an event on the northwest edge of each subcluster in Figures 9 or 10 as a front event. We measured distances from these front events to the initiation event (circle in Figures 9 and 10) and plotted them against time in the bottom frame of Figure 11. The distance increases with time almost linearly, and a straight line fits the data with a very high correlation coefficient of 0.98. The slope of the straight line gives a growth rate of 0.22 meters per minute. The location of the centroid for each subcluster in different time frames is also used to estimate the growth rate. We can fit the centroid data with a straight line with relatively lower correlation coefficient (0.85). The centroid data result in a growth rate of 0.11 meters per minute. We estimate that the growth rate of the hydraulic fracture zone under observation ranges from 0.1 to 0.2 meters per minute in a time interval from 09:00 to 11:00, December 7, 1983. In a hydraulic fracturing experiment in Low Frio Sand between shale conducted by ARCO in Jasper county, Texas, a fracture modeling results in a growth rate of 0.4 to 0.6 meters per minute (The Atlantic Richfield Corporation, 1994). Although we realize that such a comparison may not be meaningful since the two experiments were carried out in different rock types and a different geology environment, the two results happen to be o the same order of magnitude, suggesting our estimate is in a reasonable range.

Figure 12 shows the location of the hydraulic fracture zone relative to the injection interval in wellbore EE2 during the HDR experiment 2032 in Fenton Hill, New Mexico. The injection interval was located about 170 meters below the centroid of the hydraulic fracturing zone under study. The distance between the injection interval and the fracture zone is measured to be about 250 meters. The tight seismic cluster associated with the fracture zone occurred at about 9 to 11 hours after the injection started. With these parameters, we roughly estimate the propagation velocity of the stress disturbance or the fluid flow rate to be about 0.36 to 0.46 meters per minute. These values are larger, but still comparable to our estimate of the growth rate of the hydraulic fracture zone, implying that the interaction between the stress field of the pre-existing fault(s) and the stress disturbance caused by the hydraulic injection may be needed before the occurrence of the induced microearthquakes.

CONCLUSIONS AND RECOMMENDATIONS

We have developed a location approach to determine the precise source locations for microseismic events in a cluster induced during hydraulic injection. Two techniques were used in our location procedure: The waveform correlation technique was used to obtain highly accurate measurements of differential arrival times between a master event and slave events. A two-step grid search method was exploited to determine the hypocenters of microearthquakes and a refined traveltime station correction model.

Imaging of a Hydraulic Fracture

Our method was applied to a seismic waveform dataset collected during the hydraulic injection experiment 2032 at the Los Alamos HDR geothermal reservoir in Fenton Hill, New Mexico. We processed waveform data from 157 induced microearthquakes, recorded by four borehole seismic stations, to obtain a dataset of absolute and differential arrival times and determined hypocentral locations for these events. The picking error for absolute arrival time is estimated to be about 1 to 2 ms, and the reading error for differential arrival time is about 0.4 to 0.8 ms. The absolute location error is about 30 to 39 meters, which is the uncertainty relative to the true location of an event. The relative location error, which reflects uncertainty of one event location compared to those of nearby events, is estimated to be 3 to 9 meters. Our results show that the use of differential arrival time data can result in a more accurate image of a microearthquake cluster.

The hypocenter locations of 147 microearthquakes define a roughly planar cluster of about 40 meters dimension, consistent with events occurring on a near vertical fracture zone, which may be located on the pre-existing fault(s) or joint(s). The distribution of the induced seismicity allows us to determine the geometry parameters of the hydraulic fracture zone. Height and length are measured to be 35 and 40 meters, respectively, and the fracture azimuth is $N40^oW$. Analysis of temporal-spatial variation of the induced seismicity provides a tool to study the dynamic growth process of the hydraulic fracture zone. We find out that the fracture zone grows rapidly during a two-hour interval from 09:00 to 11:00. The growth rate for the length of the fracture zone ranges from 0.1 to 0.2 meters per minute.

In order to obtain a better understanding of the growth process of the hydraulic fracture zone and its mechanical properties, further investigations are required in the following aspects. Fracture modeling has to be done for the hydraulic fracturing in the Los Alamos HDR site and must be compared with the location results. The injection time history during experiment 2032 should be compared with the temporal-spatial variation of induced seismicity. The rupture size of a single induced seismic event should be reliably estimated and its relation to the size of a fracture zone should be examined. Spatial and temporal distribution of the energy released by the induced microearthquakes should reveal some mechanical properties of the hydraulic fracturing process. Successful accomplishment of these investigations will shed more light on the dynamic growth of a hydraulic fracture zone.

ACKNOWLEDGMENTS

We thank Drs. Scott Phillips and Mike Fehler for providing the seismic waveform data and other information needed to obtain our microearthquake results for the Los Alamos geothermal site. We are grateful to Dr. William Rodi for his helpful discussion. This research was supported by the ERL Borehole Acoustics and Logging Consortium and DOE grant DE-FG02-86ER13636.

REFERENCES

Albright, J.N., and C.F. Person, 1982, Acoustic emission as a tool for hydraulic fracture location: Experience at the Fenton Hill Hot Dry Rock site, *J. Soc. Pet. Eng., 22,* 523–530.

Block, L.V., 1991, Joint hypocenter-velocity inversion of local earthquake arrival time data in geothermal regions, Ph.D. thesis, Massachusetts Institute of Technology.

Block, L.V., C.H. Cheng, M.C. Fehler, and W.S. Phillips, 1993, Seismic imaging using microearthquakes induced by hydraulic fracturing, *Geophysics, 59,* 102–112.

Cash, D.J., E.F. Homuth, H. Keppler. C. Pearson, and S. Sasaki, 1983, Fault plane solutions for microearthquakes induced at the Fenton Hill, Hot Dry Rock geothermal site: Implications for the state of stress near a Quaternary volcanic center, *Geophys. Res. Lett., 10,* 1141–1144.

Deichmann, N. and M. Garcia-Fernandez, 1992, Rupture geometry form high-precise relative hypocenter locations of microearthquake clusters, *Geophys. J. Int., 110,* 501–517.

Fehler, M., L. House and H. Kaieda, 1987, Determining planes along which earthquakes occur: Method and application to earthquakes accompanying hydraulic fracturing, *J. Geophys. Res., 92,* 9407–9414.

Fehler, M. and W.S. Phillips, 1991, Simultaneous inversion for Q and source parameters of microearthquakes accompanying hydraulic fracturing in granitic rock, *Bull. Seism. Soc. Am., 81,* 553–575.

Frankel, A., 1982, Precursors to a magnitude 4.8 earthquake in the Virgin Islands: Spatial clustering of small earthquakes, anomalous focal mechanisms and earthquakes doublets, *Bull. Seism. Soc. Am., 72,* 1277–1294.

Fremont, M.J. and S.D. Malone, 1987, High precision relative locations of earthquakes at Mount St. Helens, Washington, *J. Geophys. Res., 92,* 1022–1023.

Geller, R.J. and C. S. Meuller, 1980, Four similar earthquakes in central California, *Geophys. Res. Lett., 7,* 821–824.

Harlow, F.H., and W.E., Pracht, 1972, A theoretical study of geothermal energy extraction, *J. Geophys. Res., 77,* 7038–7048.

House, L., 1987, Locating microearthquakes induced by hydraulic fracturing in crystalline rock, *Geophys. Res. Lett., 14,* 919–921.

Ito, A., 1985, High resolution relative hypocenters of similar earthquakes by cross-spectral analysis method, *J. Phys. Earth, 33,* 279–294.

Jordan, T.H., and K.A. Sverdrup, 1981, Teleseismic location techniques and their application to earthquake clusters in south-central Pacific, *Bull. Seism. Soc. Am., 71,* 1105–1130.

Li, Y., C. Doll, and M.N. Toksöz, 1995, Source characterization and fault plane determinations for Mblg= 1.2 to 4.4 earthquakes in the Charleviox seismic zone, Quebec, Canada, submitted to *Bull. Seism. Soc. Am.*

Mahere, K.D., F. Mauk, 1987, Seismic wave motion for a new model of hydraulic fracture with an induced low-velocity zone, *J. Geophys. Res., 92,* 9293–9309.

Majer E.L., and T.W. Doe, 1986, Studying hydrofractures by high frequency seismic monitoring, *Intl. J. Rock Mech. and Min. Sci, 23,* 185–199.

Moriya, H., K., Nagano, and H. Niitsuma, 1993, Precise source location of AE doublets by spectral matrix analysis of triaxial hodogram, *Geophysics, 59,* 36–45.

Pechmann, J.C. and H. Kanamori, 1982, Waveforms and spectra of preshocks and aftershocks of the 1979 Imperial Valley, California, earthquake: Evidence of fault heterogeneity? *J. Geophys. Res., 87,* 10579–10597.

Phillips, W.S., L.S. House, and M.C. Fehler, 1992, Vp/Vs and the structure of microearthquake clusters, *Seismol. Res. Lett., 63,* 56–57 (abstract).

Pine, R.J., and A.S. Batchelor, 1984, Downward migration of shearing in jointed rock during hydraulic injections, *Intl. J. Rock Mech. and Min. Sci. and Geomech. Abstr., 21,* 249–263.

Poupinet, G., W.L., Ellsworth, and J. Frechet, 1984, Monitoring velocity variations in the crust using earthquake doublets: An application to the Calaveras fault, California, *J. Geophys. Res., 89,* 5719–5731.

Rodi, W., Y. Li, and C.H. Cheng, 1993, Location of microearthquakes induced by hydraulic fracturing, *Annual Report,* Borehole Acoustics and Logging Consortium, MIT, Cambridge, Massachusetts, 369–410.

Tablebi, S., and F.-H. Cornet, 1987. Analysis of the microseismicity induced by a fluid injection in a granitic rock mass, *Geophys. Res. Lett., 14,* 227–230.

The Atlantic Richfield Corporation, 1994, The deep well treatment and injection program, fracture technology field demonstration project, *Final Report,* The Atlantic Richfield Corporation, Plano, Texas, pp. 84.

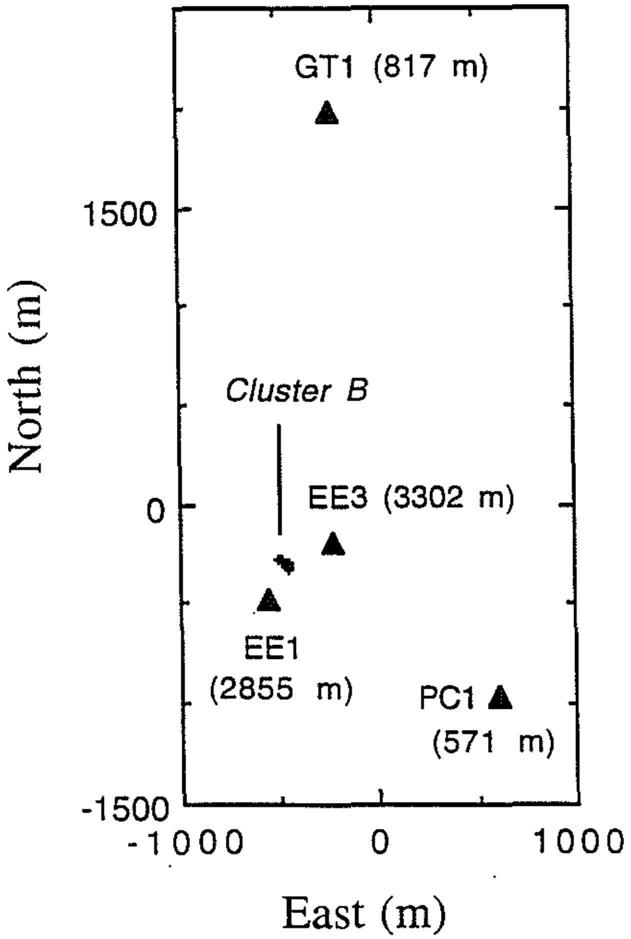

Figure 1: Map view of the geometry of borehole seismic stations and epicenters for a cluster of microearthquakes induced by hydraulic fracturing during the HDR experiment 2032 on December 7, 1983 at Fenton Hill, New Mexico. The station depths are given in parentheses.

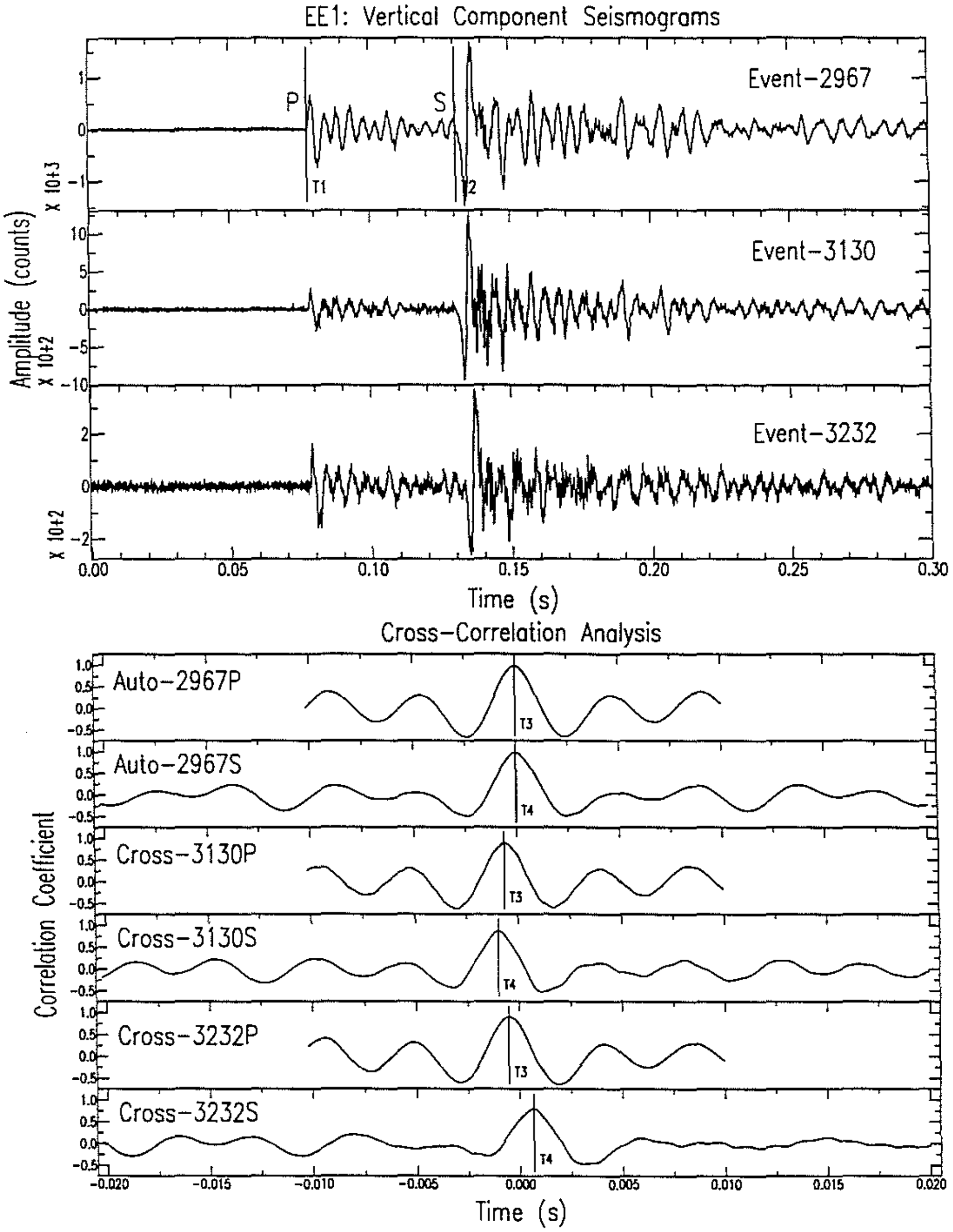

Figure 2: (Top) Vertical component seismograms of three similar microearthquakes recorded at station EE1. The vertical bars T1 and T2 indicate arrival times for P and S waves, respectively. (Bottom) Examples of differential arrival time determination from cross-correlation functions. Event 2967 is used as a master event.

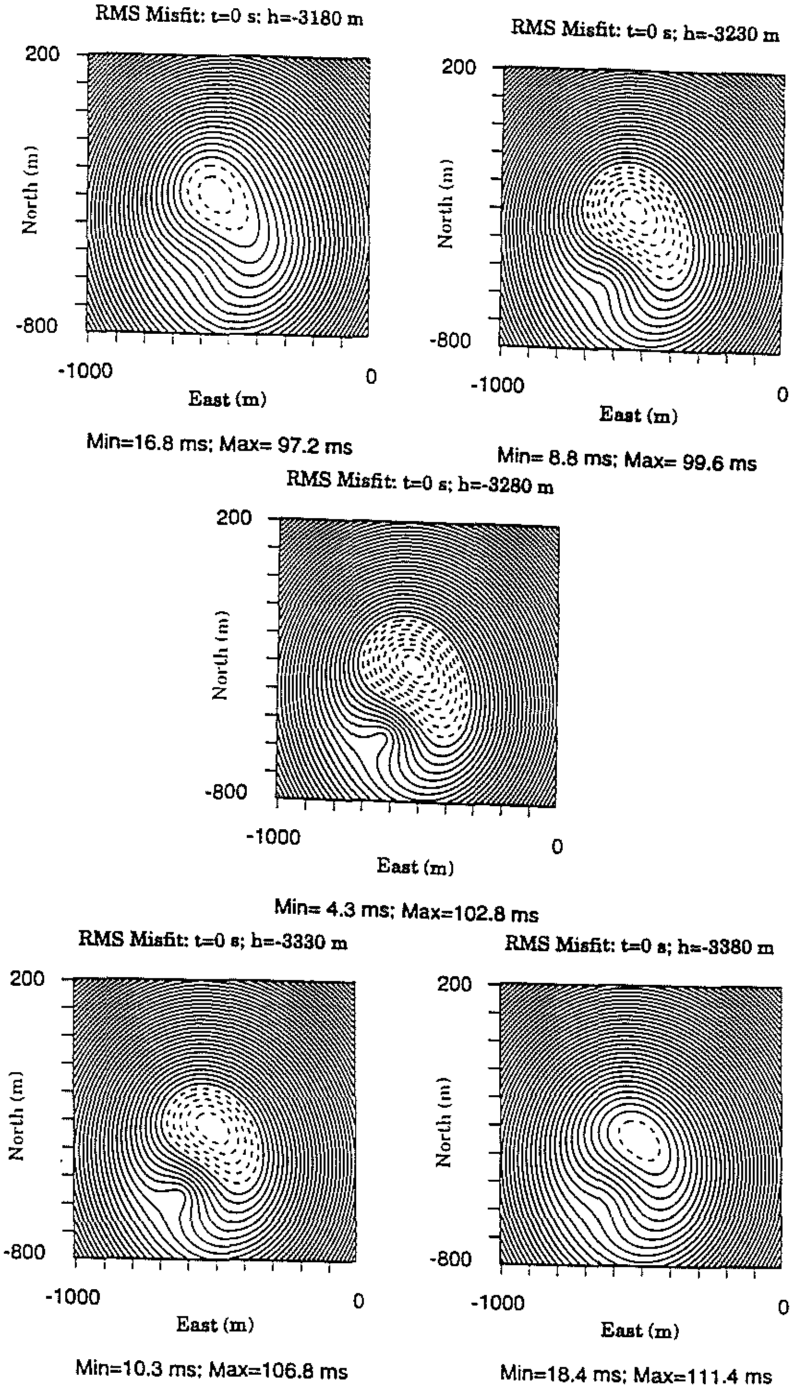

Figure 3: Contour plots of the RMS error distribution in a map view for an event at different depths. The contour interval is 2 ms. The outside dashed line in each frame corresponds to the RMS error of 20 ms. The minimum and maximum RMS misfits are shown on the bottom of each frame. The middle frame has the smallest RMS misfit, corresponding to the approximate hypocentral location of the event.

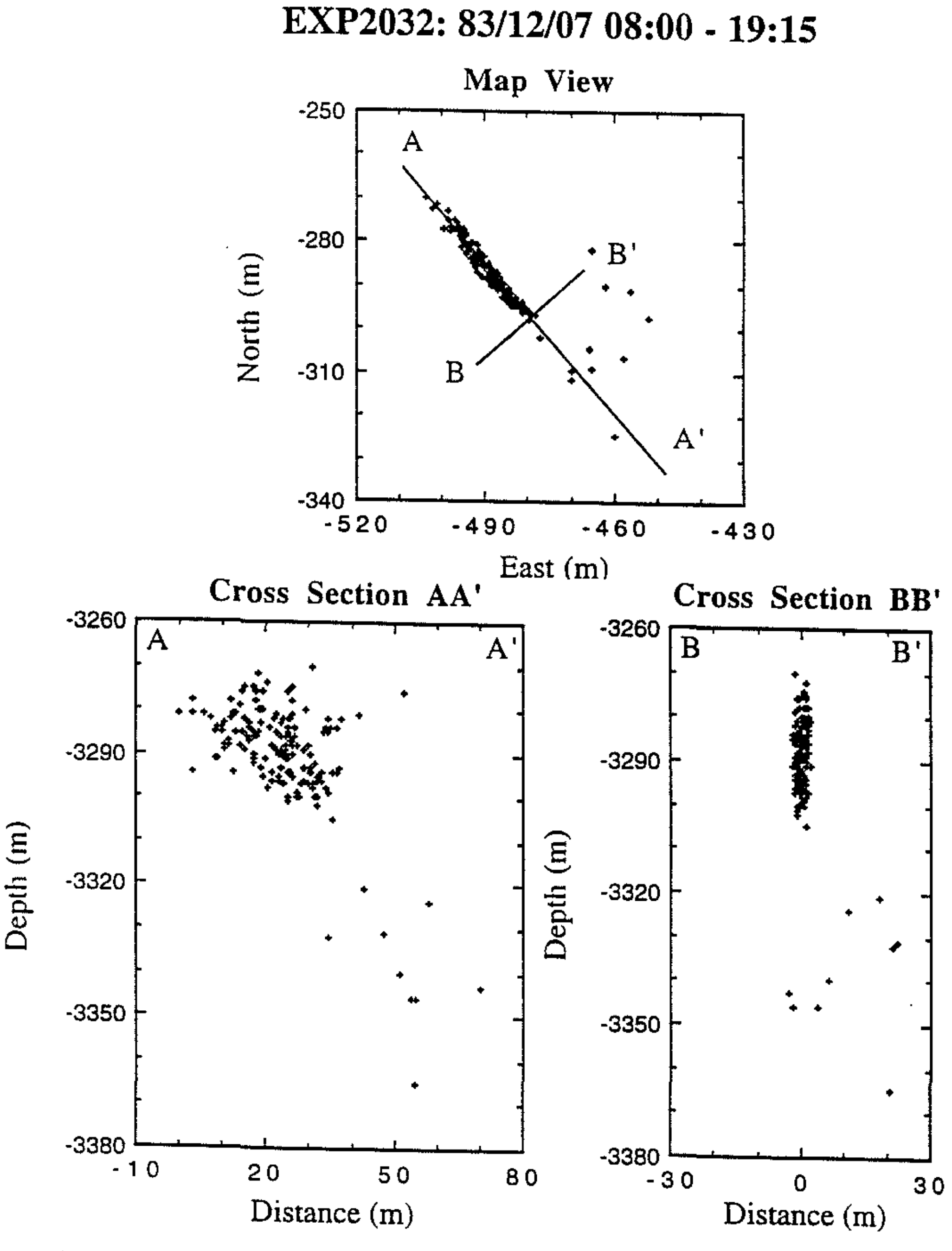

Figure 4: Map view and two vertical cross-sections showing hypocentral locations of 157 induced microearthquakes (cross). Except that a few scattering events are in the southeast, the majority of events define a hydraulic fracturing zone with the azimuth of $N40^oW$. The length and height of the fracture zone are estimated to be 40 m and 35 m, respectively.

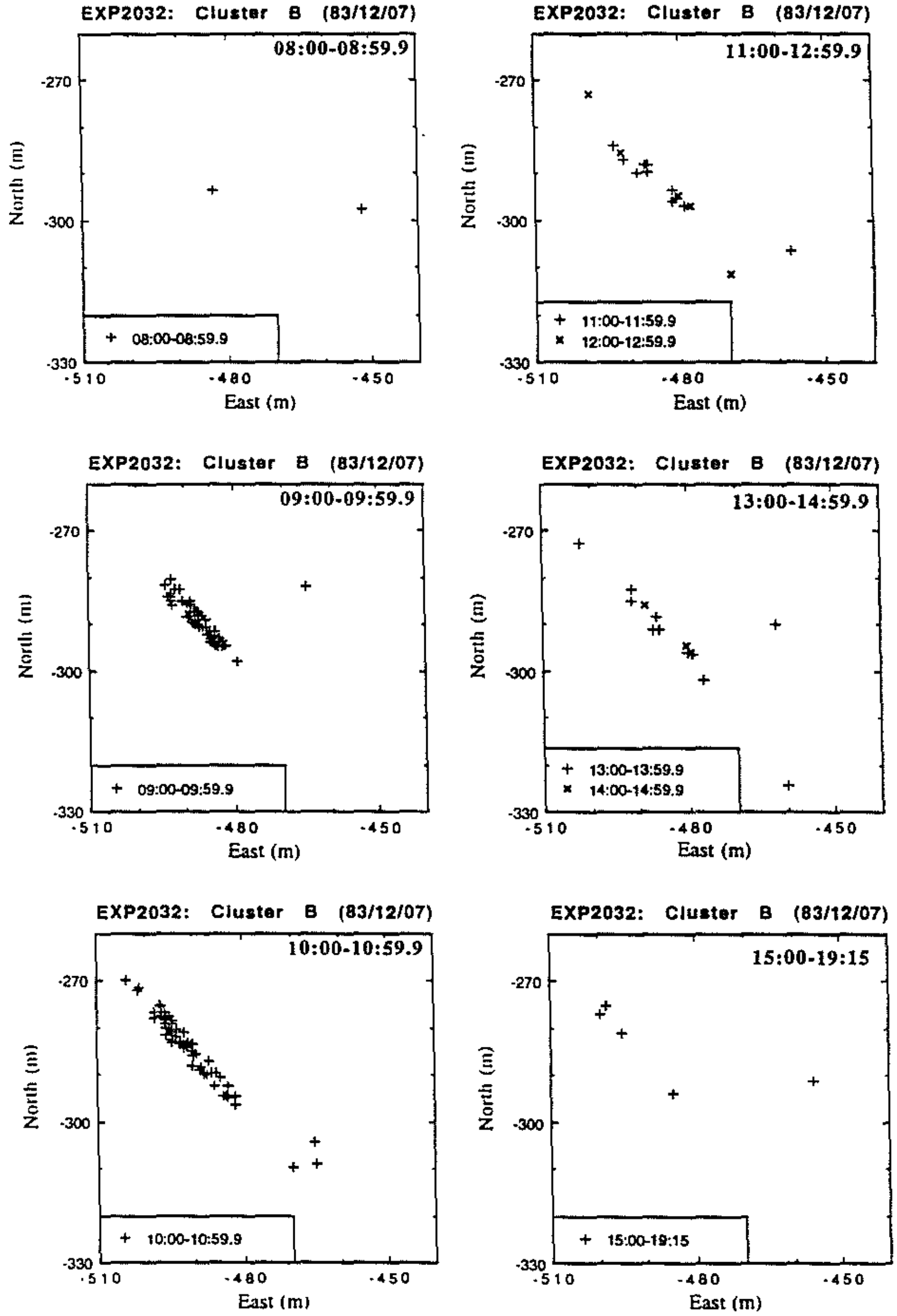

Figure 5: A series of map views showing epicentral locations for seismic events which occurred in different time windows. The majority of the events occurred during 9:00 to 11:00, December 7, 1983. The seismic activity dramatically decreased after that time.

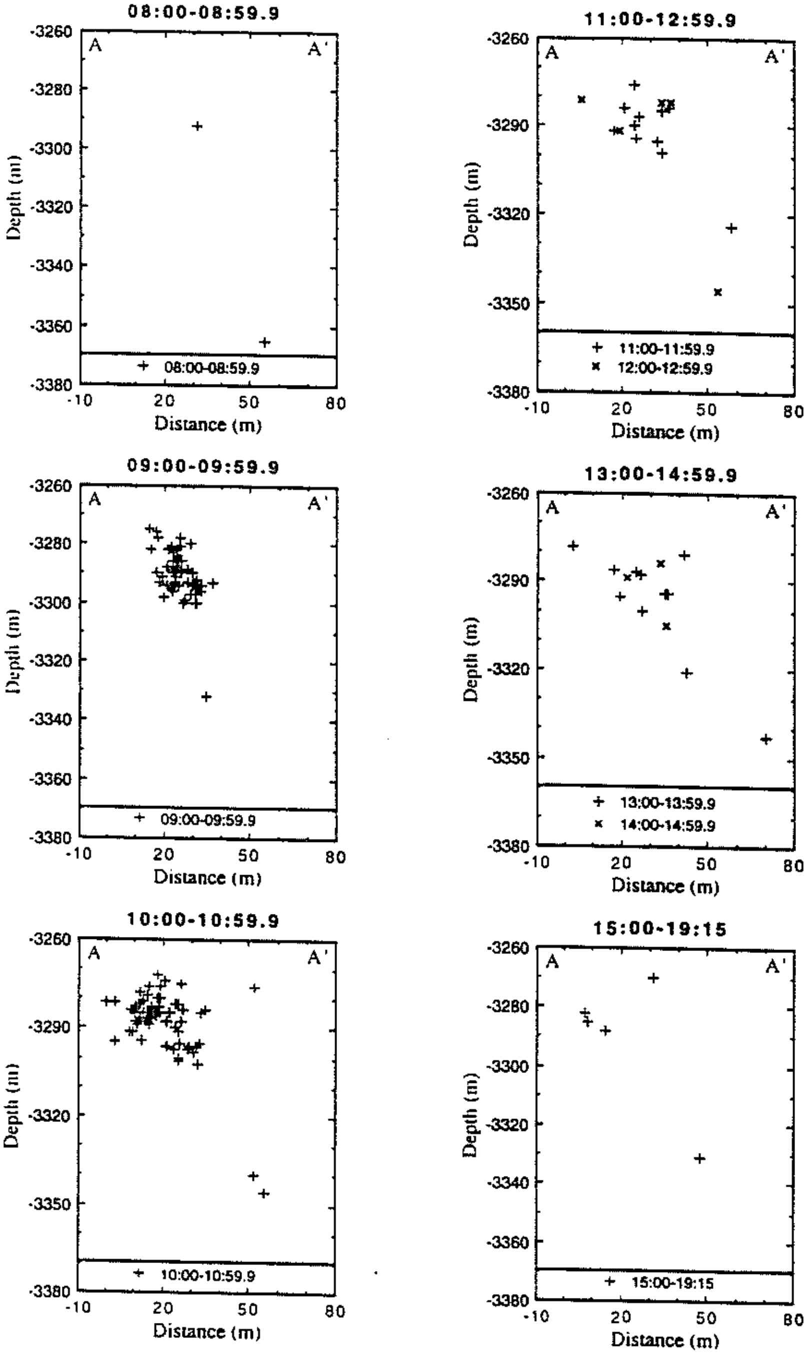

Figure 6: A series of cross-sections (AA') along the strike of the fracture zone showing hypocentral locations of seismic events which occurred in different time windows.

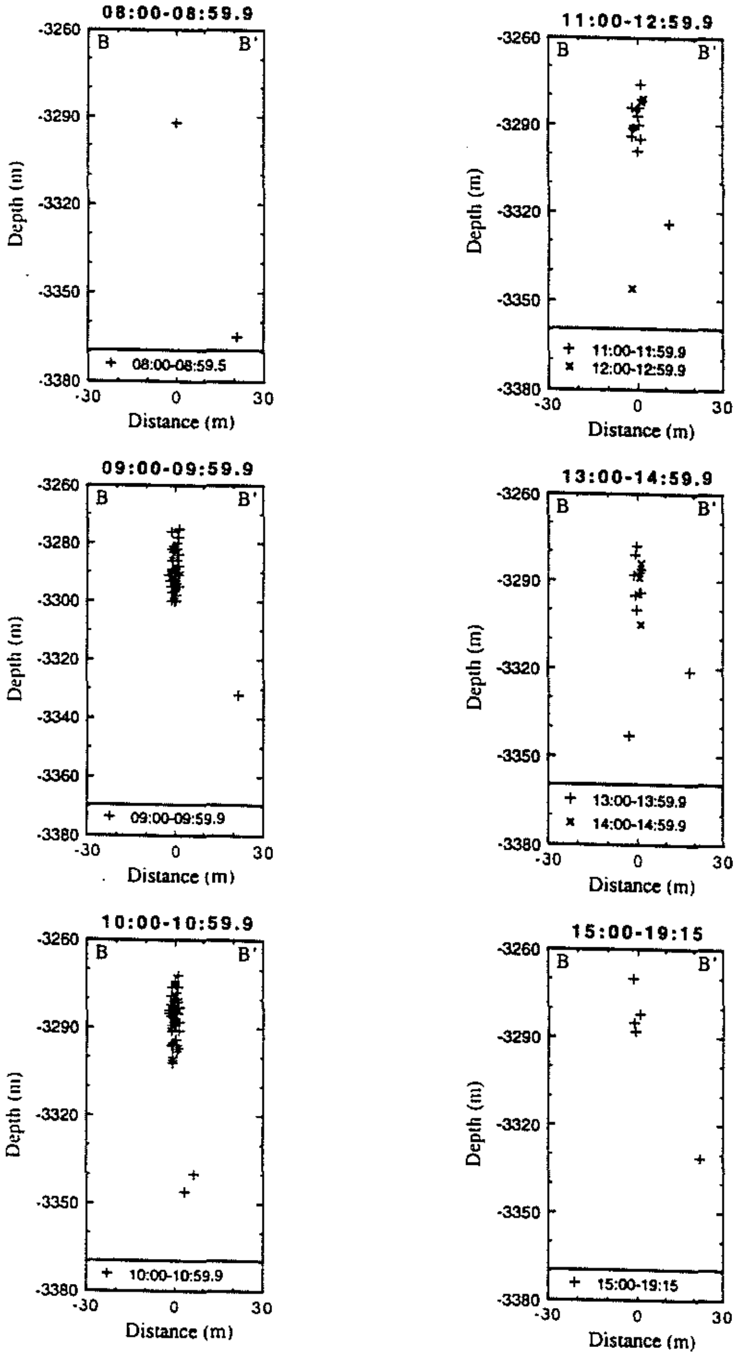

Figure 7: A series of cross-sections (BB') perpendicular to the strike of the fracture zone showing hypocentral locations of events which occurred in different time windows.

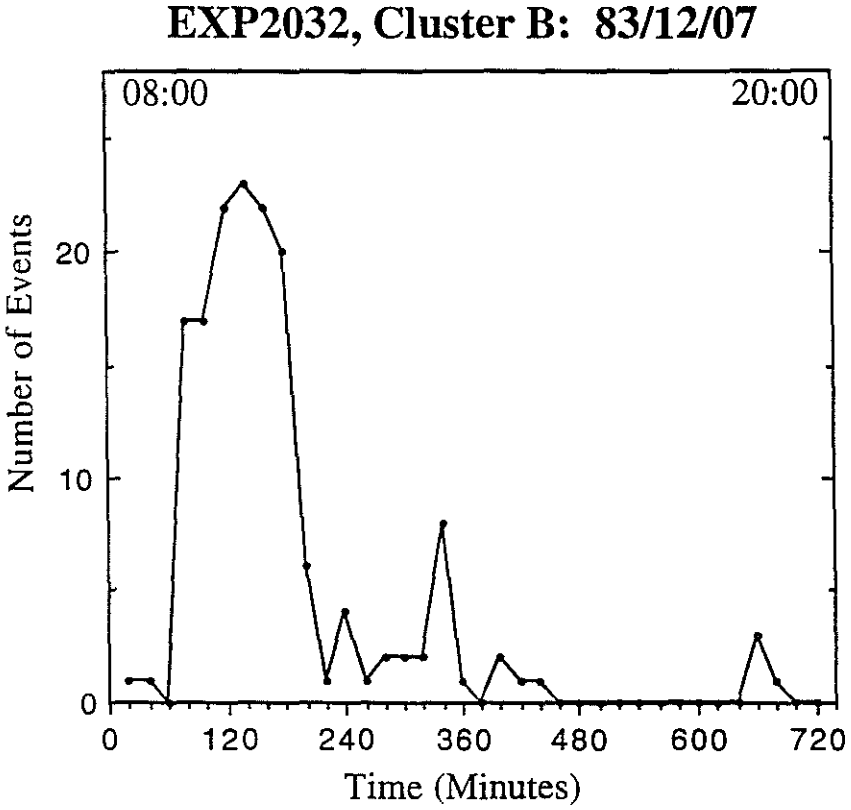

Figure 8: Frequency distribution of seismic events versus time for the cluster B. About 80% of the events occurred during 9:00 to 11:00, December 7, 1983.

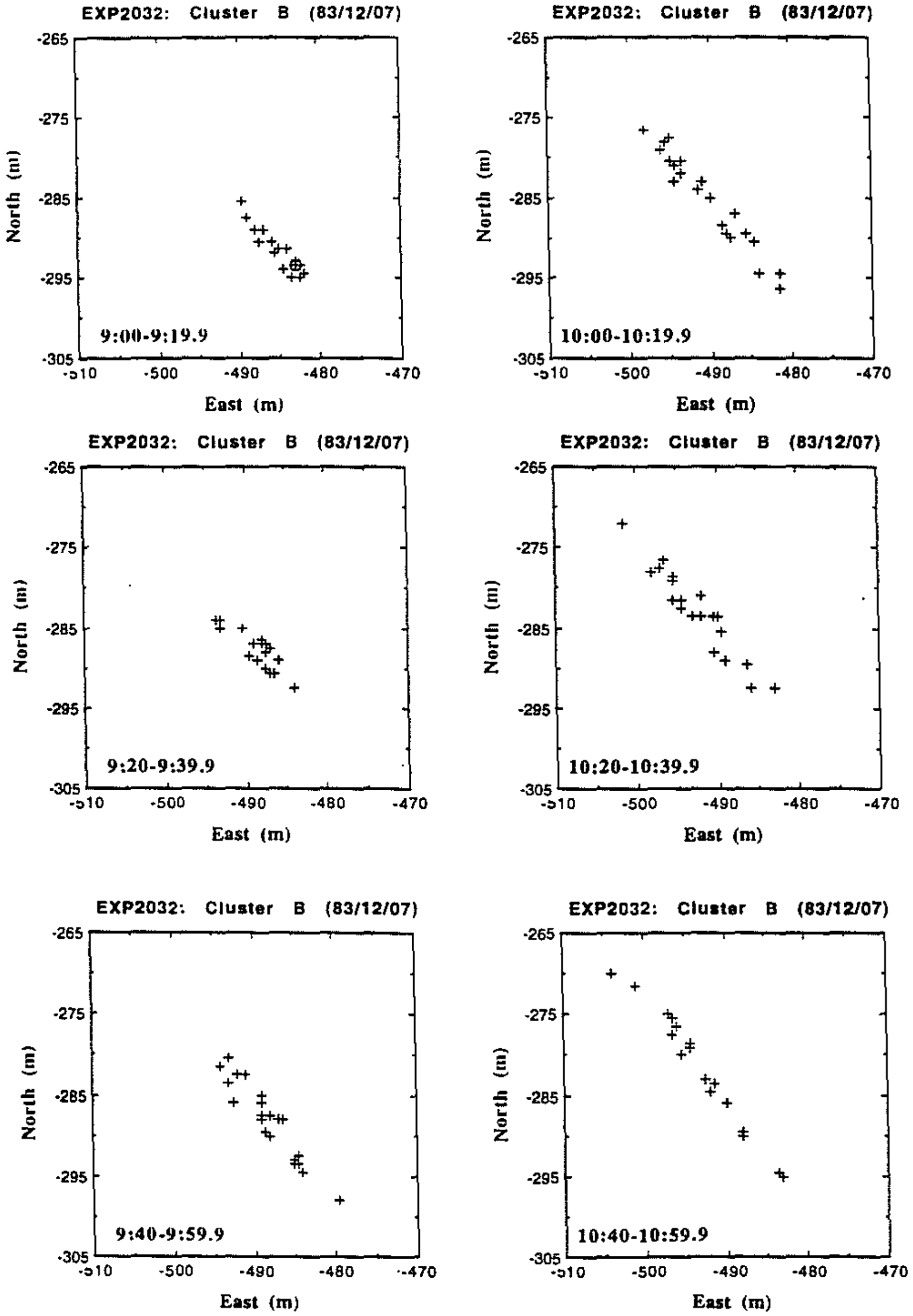

Figure 9: Map views of locations for seismic events which occurred during 9:00 to 11:00, December 7, 1983. The time window for each frame is 20 minutes. The circle represents the first event (occurred at 08:26) within the fracture zone. These plots show the growth process of the fracture zone.

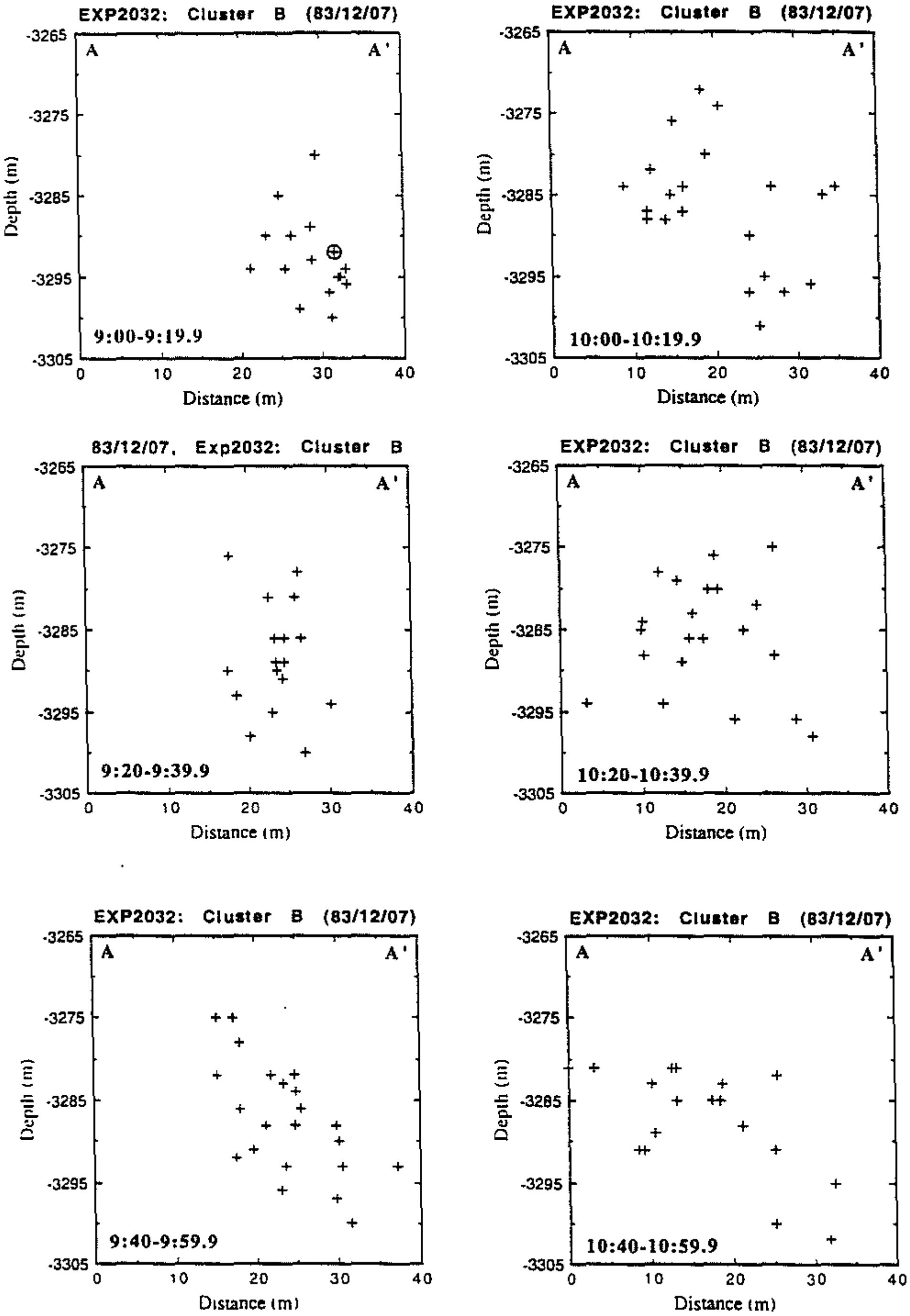

Figure 10: AA' cross-section (along the strike of the fracture zone) showing hypocentral location variations during 9:00 to 11:00, December 7, 1983. The time window for each plot is 20 minutes. The circle represents the first event (occurring at 08:26) within the fracture zone. Note that the subcluster pattern in each time frame also varies as a function of time.

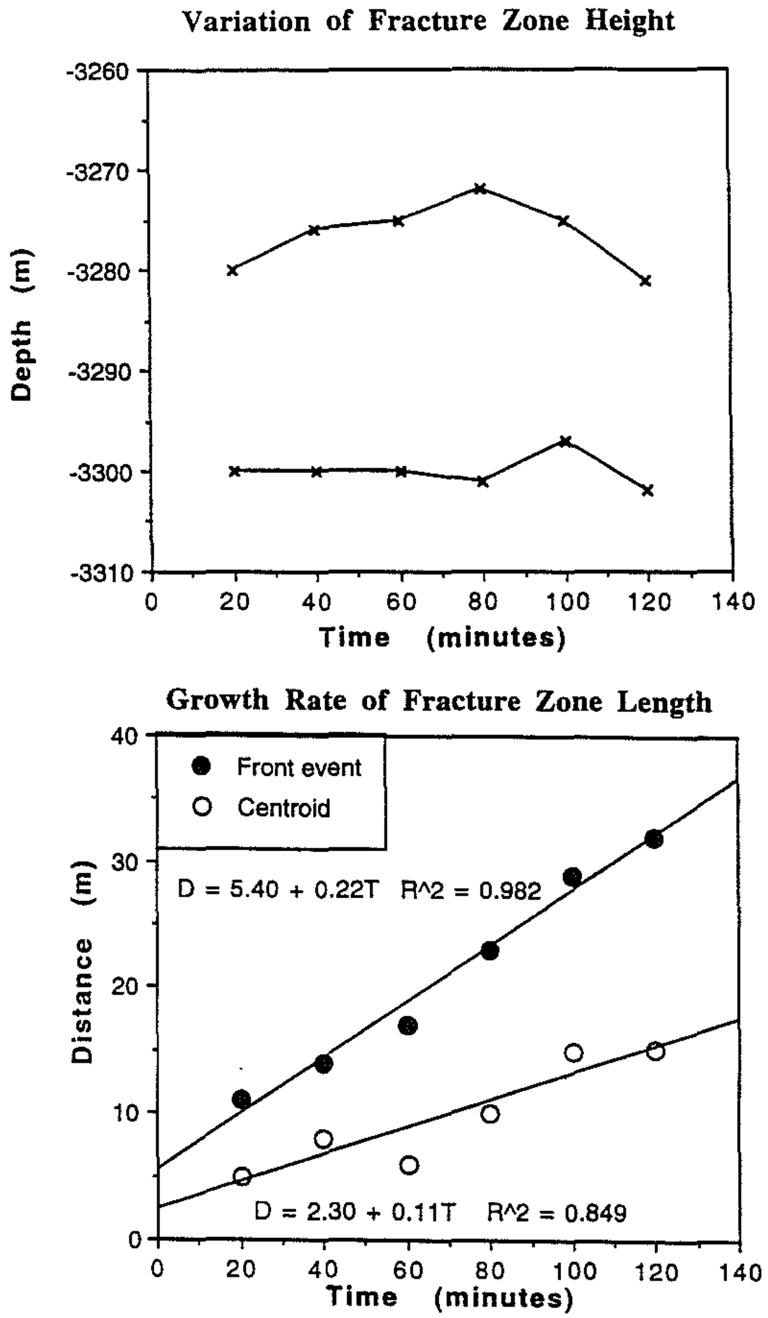

Figure 11: (Top) Temporal variation of the fracture zone height. (Bottom) Estimates of the growth rate for the fracture zone length. The front event (or centroid) in each time frame is the event on the northwest edge (or center) of each subcluster. The distance is measured from the first event (08:26) within the fracture zone. The growth rate is estimated to be 0.1 to 0.2 m per minute.

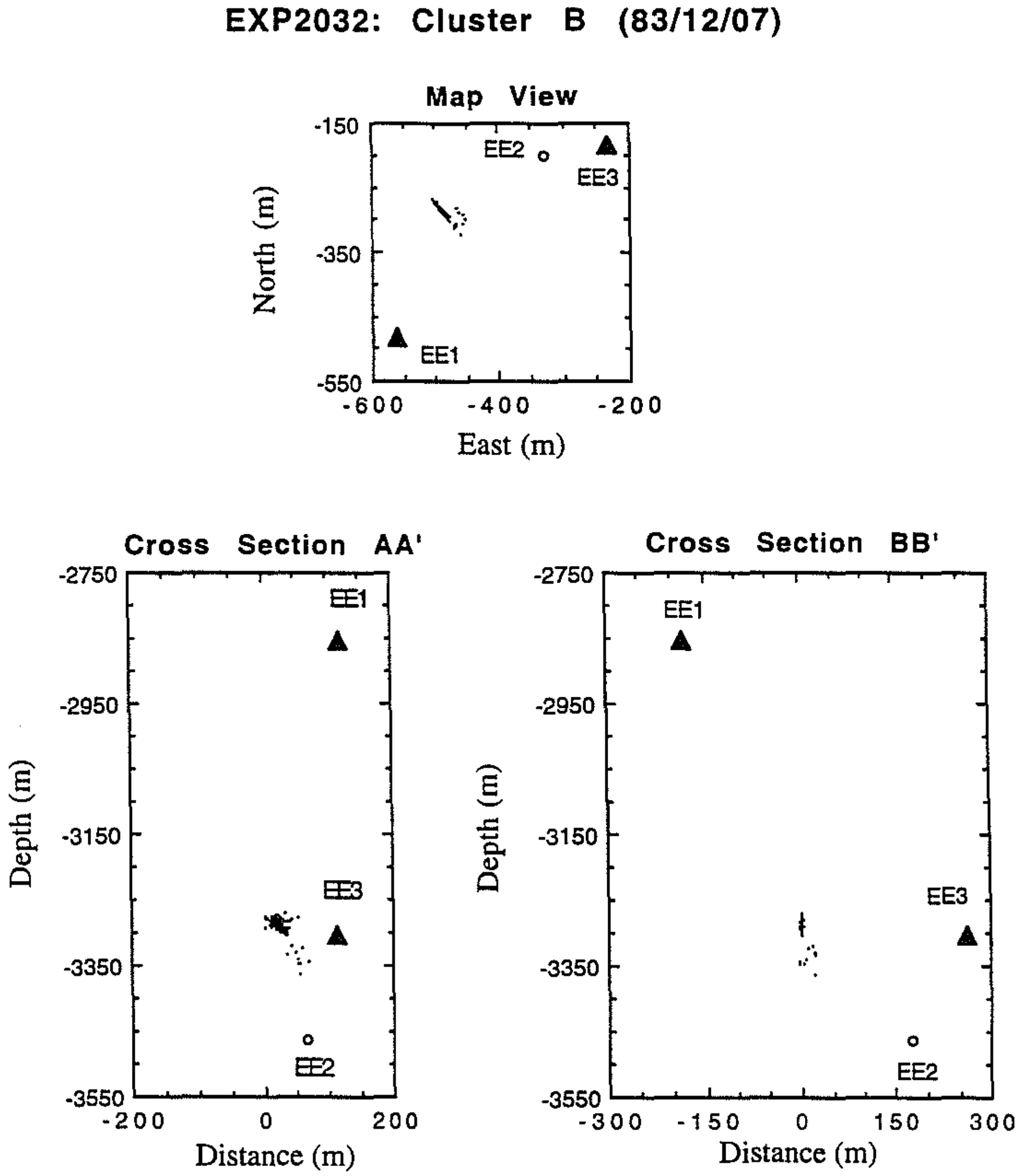

Figure 12: Orthogonal views showing the locations of microearthquakes within the hydraulic fracture zone and its vicinity, the injection interval in well EE2, and the two closest borehole seismic stations (EE1 and EE3).